Elastic reverse-time migration

Zaiming Jiang, John C. Bancroft, and Laurence R. Lines

ABSTRACT

Two aspects of elastic reverse-time migration are addressed. First, a new method of imaging conditions is proposed and compared to two popular methods. The comparison is done using a point reflector subsurface model, and the proposed method is used in migration of a shrunk Marmousi2 model. Second, a prestack reverse-time migration workflow is proposed and tested with a shrunk Marmousi2 model. The processing workflow is very different from the traditional seismic data processing workflow. For example, it is not necessary to remove ground roll from surface records.

INTRODUCTION

Reverse-time migration (RTM) is far more faithful in representing the full wave propagation phenomena than most of the other migration methods, such as Kirchhoff migration, and one-way wavefield extrapolation migration (Leveille et al., 2011).

Recent advances in technologies have made RTM commercially available, although the method was considered impractical due to its high requirements on computational resources and its sensitivity to velocity models. For example, ION's subsidiary, GX Technology (GXT), states that it commercially introduced RTM in 2005, and has used it effectively on 26 projects spread throughout the world. "Significant improvement can be achieved both in the model building and final migration by employing the two-way RTM technique. It is the combination of model building and migration that is the key to successful imaging" (Ion, 2012).

Due to high prices and increased difficulties in finding shallow deposits, exploration and exploitation of hydrocarbon resources are expected to be moving to greater depths and to deal with more complicated subearth structures. Consequently, RTM will become a more important tool.

RTM was first derived for acoustic poststack migration based on the exploding reflector model by McMechan (1983) and Whitmore (1983). Since then it has advanced to elastic prestack forms (Chang and McMechan, 1986; Sun and McMechan, 1986; Chang and McMechan, 1987; Sun and McMechan, 1988). Bording and Lines (1997) presented an excellent tutorial on modelling and RTM.

The imaging principle and imaging conditions (ICs) are the heart of RTM algorithms, and there is extensive literature available. Claerbout (1971) stated the imaging principle, "Reflectors exist at points in the ground where the first arrival of downgoing wave is time coincide with an upgoing wave", and proposed two methods for ICs, with one using a ratio of upgoing over downgoing wavefield amplitudes, and the other using cross-correlation between downgoing and upgoing wavefields, formulated in both frequency and time domains. Whitmore and Lines (1986) proposed source normalized cross-correlation method. Chang and McMechan (1987) used ray tracing. Loewenthal and Hu (1991) proposed two

methods: one is by maximum amplitude criteria, and the other is by minimum time criteria. Biondi and Shan (2002) practiced the cross-correlation method. Kaelin and Guitton (2006) proposed to normalize the cross-correlation by upgoing wavefields. Chattopadhyay and McMechan (2008) summarized several methods: excitation-time ICs, which is similar to methods of Loewenthal and Hu (1991), cross-correlation ICs, and ratio of upgoing over downgoing wavefield amplitudes. The most recent technologies on IC are developed for elastic RTM. For example, Yan and Sava (2007) presented elastic ICs based on wavefield decomposition, and Du et al. (2012) applied source normalized cross-correlation method with polarity reversal correction for elastic RTM.

The authors of this CREWES report have reported their practises on RTM (Jiang et al., 2009, 2010). Their RTM methods are based on an elastic wave modelling method, which employs a staggered-grid finite-difference scheme. A potential advantage of their RTM methods is that the methods will be more accurate on solid-liquid boundary modelling than RTM methods that are based on non-staggered-grid scheme. There are disadvantages of their methods though. For one thing, in those methods, only the vertical component of the wavefields were used in the IC methods, although an elastic wave modelling method was applied and multicomponent wavefields were available. For another, similar to most of the conventional seismic processing methods, suppressing groundroll posed as an challenge.

The first author's dissertation (Jiang, 2012) proposed a new method of elastic ICs and a unique RTM workflow, and this report is an abstract of those ideas. First, a new IC method, called energy normalized crosscorrelation ICs, is compared to two popular methods, cross-correlation IC and amplitude normalized crosscorrelation IC. The analysis is based on a point reflector subsurface model and is further verified by a shrunk Marmousi2 model. Second, a unique RTM workflow is sketched: in the new workflow, no preprocessing of groundroll is needed. The workflow is tested with a shrunk Marmousi2 subsurface model.

IMAGING CONDITIONS

Based on a point reflector subsurface model, two existing methods of ICs are discussed, and a new method is proposed.

A point reflector subsurface model

A 2D subsurface model contains a point reflector in a homogeneous medium in x_1-x_3 plane is built. The P-wave velocity is shown in Figure 1. The parameters used in P-SV modelling are Lamé parameters and density. These parameters are derived from the P-wave velocities. For details, please refer to Jiang (2012).

Cross-correlation IC without normalization

An IC for an acoustic RTM method is a zero-lag cross-correlation of source waves and receiver wavefields (Claerbout, 1971; Biondi and Shan, 2002)

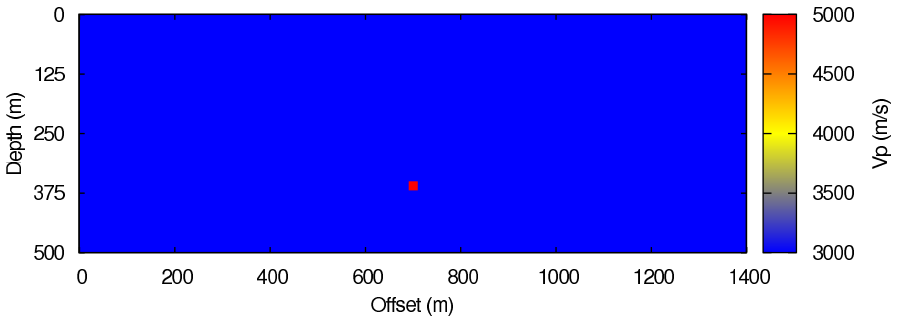

FIG. 1: A point reflector model.

$$Image(x_1, x_3) = \sum_t S(x_1, x_3, t) R(x_1, x_3, t), \tag{1}$$

where $S(x_1, x_3, t)$ and $R(x_1, x_3, t)$ are, respectively, the source and receiver wavefields. The cross-correlation term $S(x_1, x_3, t)R(x_1, x_3, t)$ at a certain time looks like a snapshot shown on the right column of Figure 2. Thus the imaging condition for a shot gather in equation 1 is implemented by stacking all the cross-correlation snapshots.

For a multicomponent algorithm, there are both horizontal and vertical components for both source and receiver wavefields. Thus, one can actually have four cross-correlation ICs:

$$I_{VV}(x_1, x_3) = \sum_t S_V(x_1, x_3, t) R_V(x_1, x_3, t), \tag{2a}$$

$$I_{VH}(x_1, x_3) = \sum_t S_V(x_1, x_3, t) R_H(x_1, x_3, t), \tag{2b}$$

$$I_{HV}(x_1, x_3) = \sum_t S_H(x_1, x_3, t) R_V(x_1, x_3, t), \tag{2c}$$

$$I_{HH}(x_1, x_3) = \sum_t S_H(x_1, x_3, t) R_H(x_1, x_3, t), \tag{2d}$$

where subscripts V and H denotes, respectively, vertical and horizontal components. Hereafter the ICs will be referred to as VV, VH, HV, and HH ICs.

Figure 3 shows RTM images from the shot shown in Figure 2. As stated in the paper by Claerbout (1971), the imaging energy "drops off rapidly in any region where either the downgoing wave is weak or the upgoing wave is weak". This is a desirable property. First, for regions where the downgoing wave is time coincident with the upgoing wave, there is imaging energy; second, for stronger coincidence, there is stronger imaging energy. However, for the regions close to the seismic energy source point, where the downgoing wave, or source wavefield, is very strong, the imaging energy becomes very high. This source effect of imaging is not a desirable property. This is referred hereafter as 'strong-source effect' of cross-correlation ICs, in order to distinguish this kind of source effect from another kind of source effect described in the next subsection. Strong-source effect can be observed in Figure 3a, 3b, and 3c.

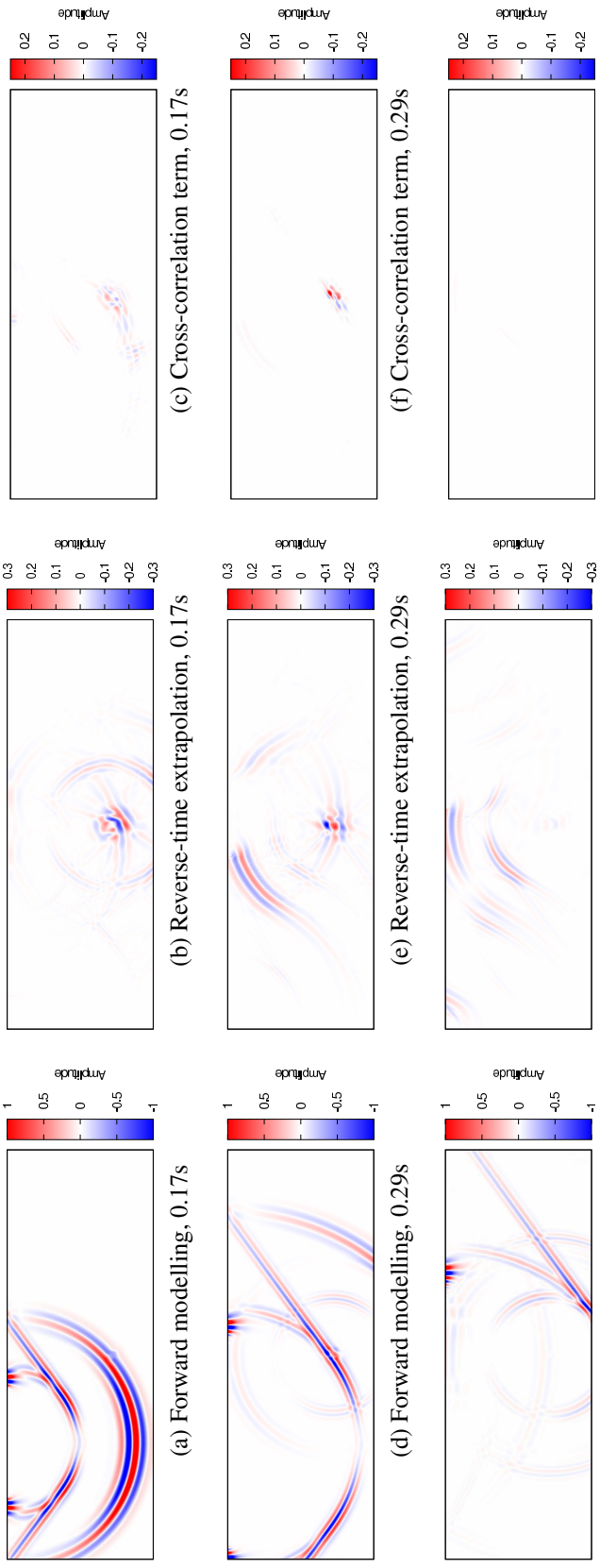

FIG. 2: Forward modelling and reverse-time extrapolation of P-SV waves, and their cross-correlation. The modelling is done with a surface source which is horizontally far away from the surface centre. This is the vertical component.

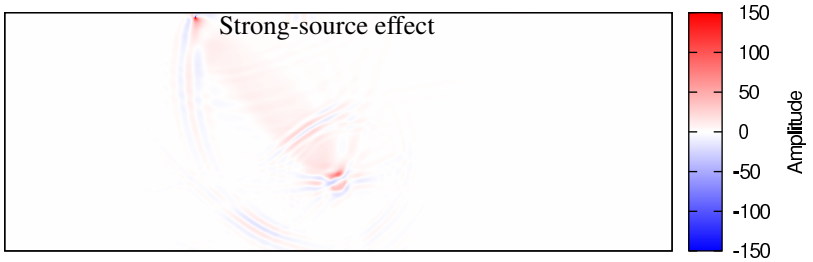

(a) VV

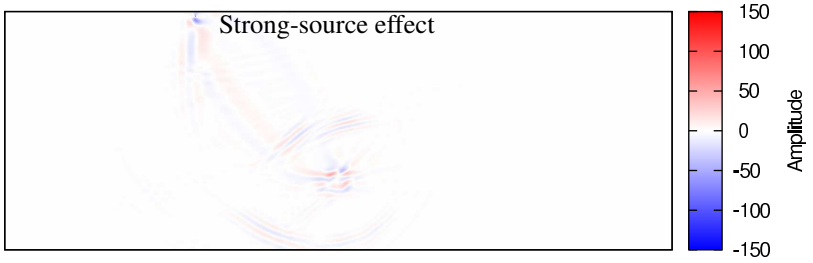

(b) VH

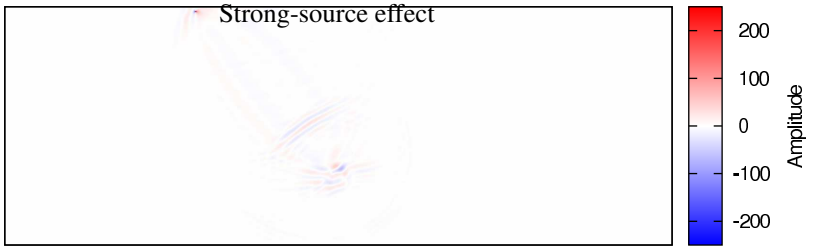

(c) HV

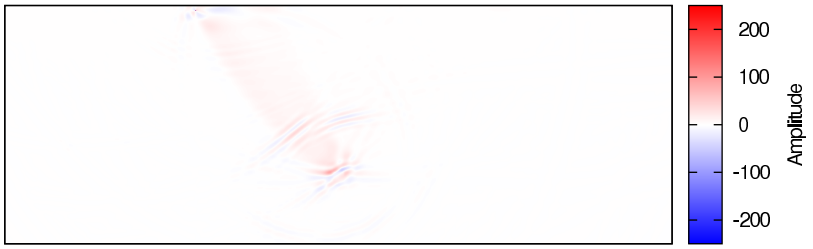

(d) HH

FIG. 3: Far-away source shot imaging result of cross-correlation without normalization.

Source normalized cross-correlation ICs

A source normalized cross-correlation IC for an acoustic shot gather is given as (Whitmore and Lines, 1986; Kaelin and Guitton, 2006; Chattopadhyay and McMechan, 2008)

$$Image(x_1, x_3) = \frac{\sum_t S(x_1, x_3, t) R(x_1, x_3, t)}{\sum_t S^2(x_1, x_3, t)}. \tag{3}$$

Obviously, when implementing the IC, one needs to avoid the problem of division by zero. One technique is to use an additive constant in the denominator. Another method is based on a threshold: if the denominator or the numerator is less than a certain threshold, the imaging result is set to zero. Here a threshold for the denominator is used.

Because the source wavefield auto-correlation term is used as the denominator on the right, for regions close to the shot point, the imaging energy will be brought down. Hence, the strong-source effect is suppressed.

For a multicomponent algorithm, Du et al. (2012) re-wrote the above IC to four equations as follows.

$$I_{VV}(x_1, x_3) = \frac{\sum_t S_V(x_1, x_3, t) R_V(x_1, x_3, t)}{\sum_t S_V^2(x_1, x_3, t)}, \tag{4a}$$

$$I_{VH}(x_1, x_3) = \frac{\sum_t S_V(x_1, x_3, t) R_H(x_1, x_3, t)}{\sum_t S_V^2(x_1, x_3, t)}, \tag{4b}$$

$$I_{HV}(x_1, x_3) = \frac{\sum_t S_H(x_1, x_3, t) R_V(x_1, x_3, t)}{\sum_t S_H^2(x_1, x_3, t)}, \tag{4c}$$

$$I_{HH}(x_1, x_3) = \frac{\sum_t S_H(x_1, x_3, t) R_H(x_1, x_3, t)}{\sum_t S_H^2(x_1, x_3, t)}, \tag{4d}$$

where a denominator uses the same component of source wavefield in the numerator.

Figure 4 shows the resulting images. Comparing these images to those shown in Figure 3, one can observe that the imaging energy close to the shot point has gone, i.e., strong-source effect is suppressed.

However, there is another kind of source effect. Figure 4c and 4d show high imaging energy right below the seismic energy source position. This is caused by the fact that the horizontal component of the downgoing wave is very weak: the incident P wavefront right under the source causes no or very weak horizontal vibrations of rock particles, and the incident S wave front right under the source causes no or very weak vibrations (horizontal or vertical) either. This is referred to as 'weak-source effect' of source normalized ICs.

Some methods have been tried to suppress the weak-source effect within the frame of source normalized cross-correlation IC. One method is to detect surrounding energy level, and decide an imaging threshold to avoid the false imaging. The method works well, especially when the source and the reflector are not in the same horizontal range. However, the method presented in the next subsection is a more general solution to the weak-source effect problem.

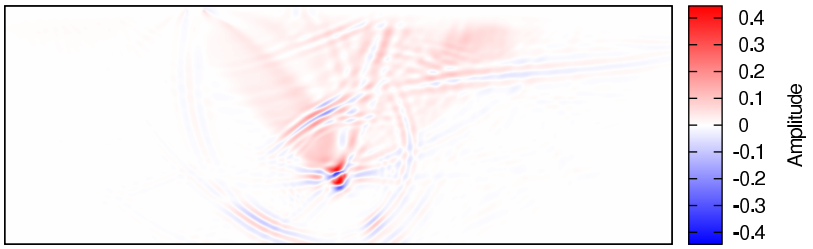

(a) VV

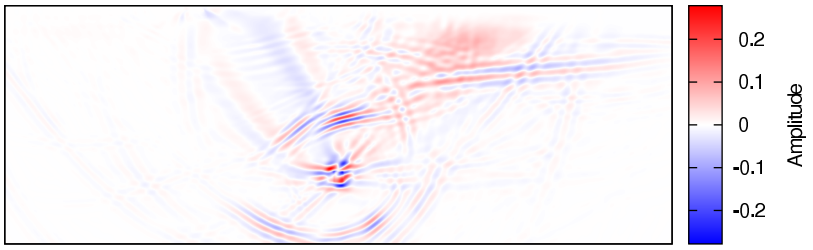

(b) VH

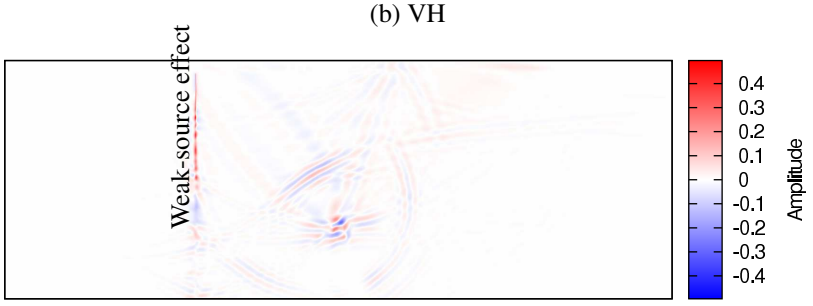

(c) HV

(d) HH

FIG. 4: Far-away source shot imaging result of cross-correlation with source normalization.

Source energy normalized cross-correlation ICs

In order to suppress the weak-source effect, a new set of ICs is proposed as follows.

$$I_{VV}(x_1,x_3)=\frac{\sum_t S_V(x_1,x_3,t)R_V(x_1,x_3,t)}{\sum_t (S_V^2(x_1,x_3,t)+S_H^2(x_1,x_3,t))}, \tag{5a}$$

$$I_{VH}(x_1,x_3)=\frac{\sum_t S_V(x_1,x_3,t)R_H(x_1,x_3,t)}{\sum_t (S_V^2(x_1,x_3,t)+S_H^2(x_1,x_3,t))}, \tag{5b}$$

$$I_{HV}(x_1,x_3)=\frac{\sum_t S_H(x_1,x_3,t)R_V(x_1,x_3,t)}{\sum_t (S_V^2(x_1,x_3,t)+S_H^2(x_1,x_3,t))}, \tag{5c}$$

$$I_{HH}(x_1,x_3)=\frac{\sum_t S_H(x_1,x_3,t)R_H(x_1,x_3,t)}{\sum_t (S_V^2(x_1,x_3,t)+S_H^2(x_1,x_3,t))}. \tag{5d}$$

The denominators on the right are the sum of zero-lag auto-correlation of both source components. This is expected to help reduce the weak-source effect. Also, it makes more sense to use the whole source wave energy as the denominator than to use only one component: the reflections are caused by the whole source wave instead of one component, after all.

The acoustic IC (Equation 3) is expected to extrapolate the acoustic reflection coefficients (Claerbout, 1971). Correspondingly, each of the four ICs in Equation 5 can be interpretated as a linear combination of the PP, PS, SP, SS reflection coefficients, and each IC is a brute approximation of the reflection coefficients: VV IC is an approximation of PP reflection coefficients, VH is of PS, and so on.

Since the right sides of the four equations in equation system 5 have the same denominator, it is reasonable to try to stack the four images together as follows.

$$\begin{aligned} &Image(x_1,x_3)\\ =&I_{VV}(x_1,x_3)+I_{VH}(x_1,x_3)+I_{HV}(x_1,x_3)+I_{HH}(x_1,x_3)\\ =&\frac{\sum_t(S_VR_V+S_VR_H+S_HR_V+S_HR_H)}{\sum_t(S_V^2+S_H^2)}. \end{aligned} \tag{6}$$

where S_V,S_H, R_V, and R_H are all functions of (x_1,x_3,t). The stacking operator in the above equation seems to be unclear in physical meanings, but it leads to sharper and clearer imaging of subsurface structures, as shown later.

The sum of zero-lag auto-correlation of both source components has the physical interpretation of the wave energy. Thus, the above five equations are referred to as 'source energy normalized cross-correlation ICs'.

There are advantages of source energy normalized ICs. On one hand, comparing to the ICs without normalization (Figure 3), the source energy normalized ICs do not lead to a strong-source effect. On the other hand, comparing to the source normalized ICs (Figure 4), the source wave energy, instead of one component of the wave, avoids the weak-source effect. In addition, the source energy normalized ICs result in images with higher signal-to-noise ratio which can be easily recognized.

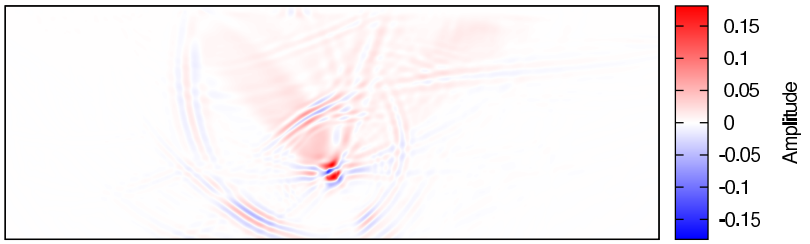

(a) VV

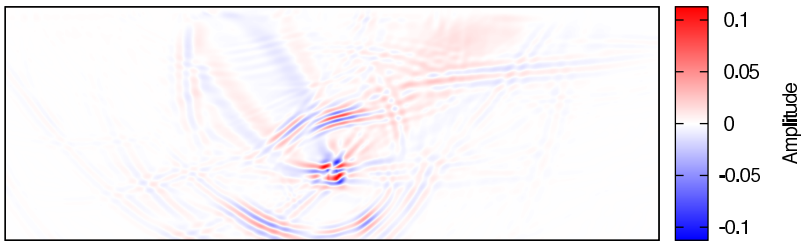

(b) VH

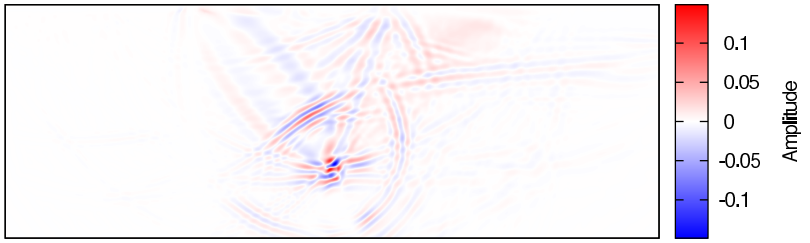

(c) HV

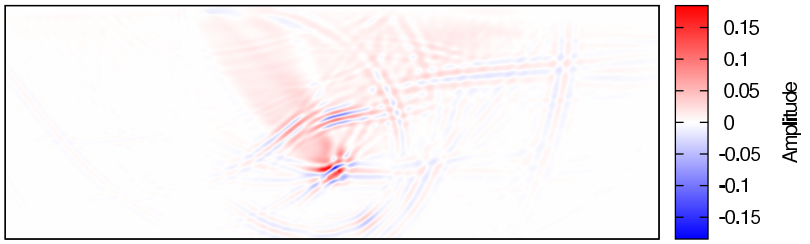

(d) HH

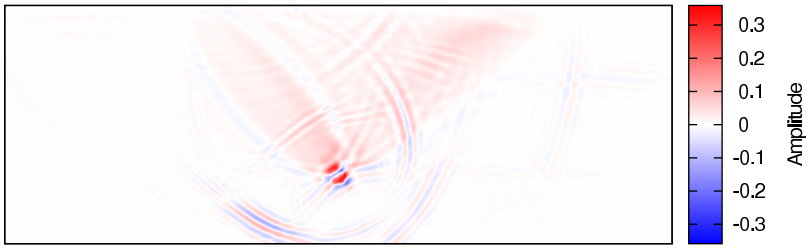

(e) Stack of above four images

FIG. 5: Far-away source shot image with source energy normalization.

All the four multicomponent ICs in Equations 5 images the point reflector to some extent, while each of them has its own characteristics (Figure 5). First, generally speaking, the imaging quality of the IC in Equation 5a (VV IC), which is resulted from the use of the vertical component of source wavefield and the vertical component receiver wavefield, is the best (Figure 5a). Second, ICs in Equations 5a and 5d (HH IC) result in relatively higher vertical resolution than horizontal one, while ICs in Equations 5b (VH IC) and 5c (HV IC) result in higher horizontal resolution than vertical one. Some researchers, such as Du et al. (2012), try some techniques to apply polarity reversal correction in ICs. In our point of view, that correction hurts the image resolution, especially the horizontal resolution.

The IC in Equation 6 (stacking IC) results in even better image quality (Figure 5e). First, the overall imaging energy is the highest and the highest amplitudes are more focused on the point reflector better (see the legends in Figure 5e, in which the highest amplitudes are the clip amplitudes). Second, the stacked images show both higher vertical and horizontal resolutions than all the other ICs do.

RTM WORKFLOW

Using a subsurface model extracted from the elastic Marmousi2 model, an elastic RTM workflow is presented.

A subsurface model: shrunk Marmousi2

Part of Marmousi2 is extracted and shrunk to create a much smaller subsurface model. There are 13601 horizontal nodes and 2801 vertical nodes in Marmousi2. First, the part from the grid node (3201, 405) to (10560, 2800) of the Marmousi2 model is extracted to obtain the structure. Note that the water layer is removed by this step. Then, one node from every three in both horizontal and vertical direction is extracted to obtain a down-sized Marmousi model. Now the new model has a grid of 2453×798 nodes, with a lateral length of $2066.25m$ and a depth of $997.5m$. Thus, the shrunk Marmousi model (Figure 6) keeps the complex structures of Marmousi2 model, but its size is much smaller, which has the advantage of less computational cost. However, with rock layers being shrunk to one third of the original thickness, so it is more difficult to image them.

Table 1: Wave velocity and density range of the shrunk Marmousi2 model.

Property	Low limit	High limit
P-wave velocity (m/s)	1530.56	4700.00
S-wave velocity (m/s)	311.53	2752.00
Density (kg/m^2)	1720.00	2627.00

Table 1 shows the rock property ranges for the new model. The low velocity and low density 'layers' are mainly at the shallow subsurface.

Prestack RTM workflow

Four main steps are designed for a prestack RTM workflow, as shown in Figure 7.

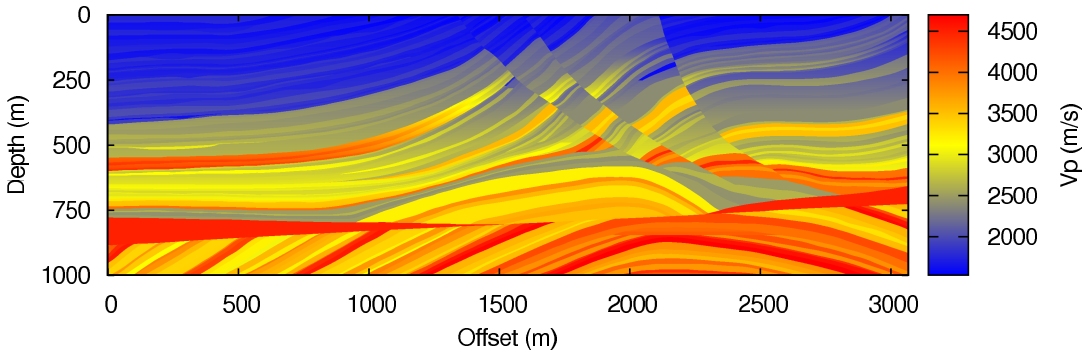

(a) P-wave velocity

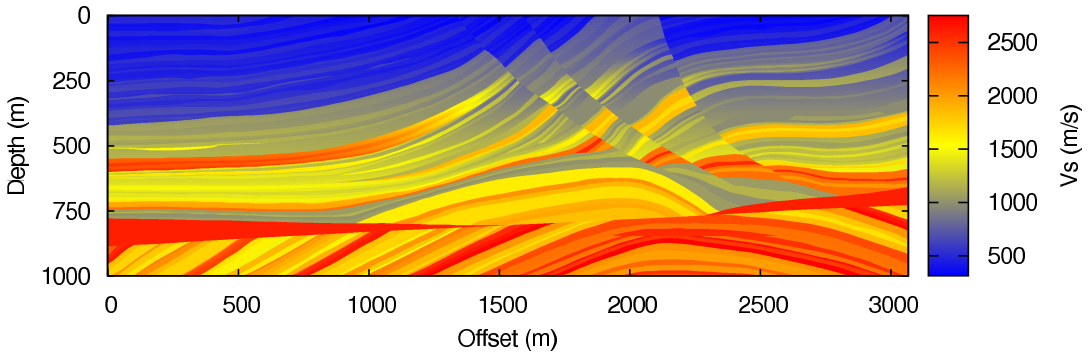

(b) S-wave velocity

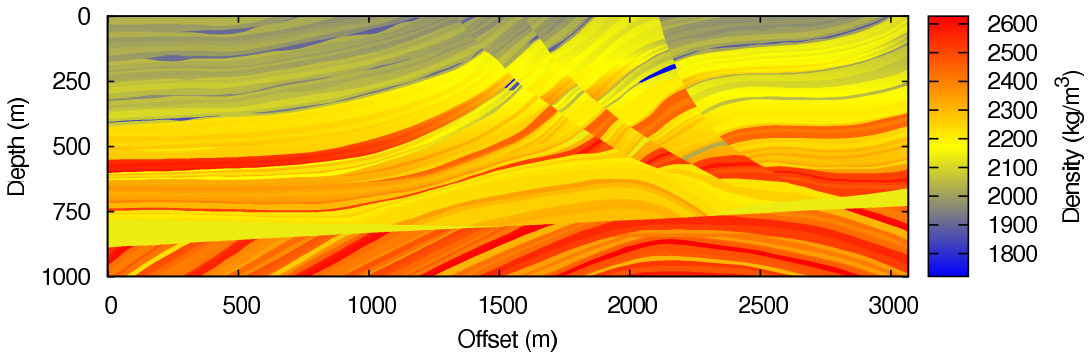

(c) Density

FIG. 6: A new elastic Marmousi model cut and shrunk from Marmousi2. Note that Water layer in the original Marmousi2 is removed.

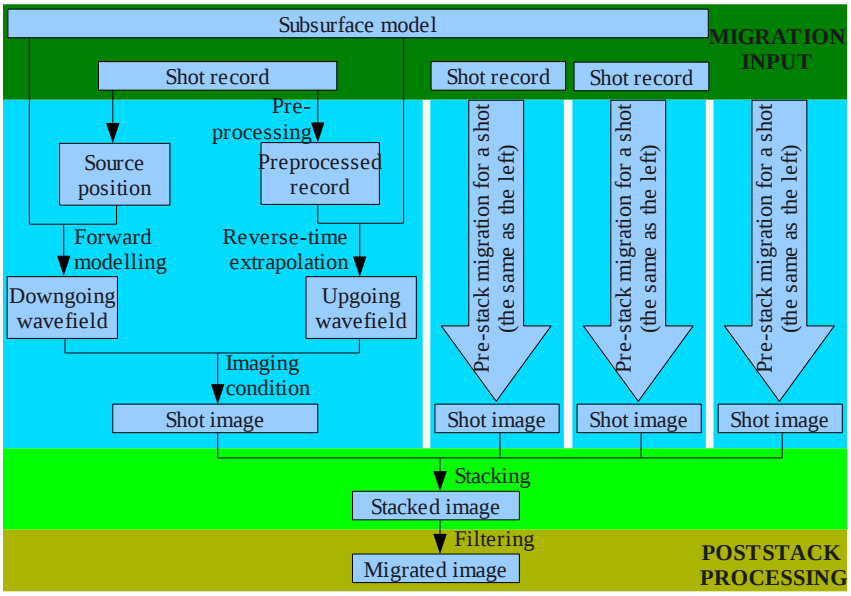

FIG. 7: Prestack RTM workflow.

Input data for migration

The first step is to acquire surface records and to build subsurface model. In a real seismic survey, surface records are acquired from seismic surveys, and a subsurface model can be built from well logs, velocity analysis from surface record, full waveform inversion, and so on. In the numerical experiment, the subsurface model is the shrunk Marmousi2 model, and the surface record is acquired from wave modelling using the shrunk Marmousi2 model.

It is easy to recognize some common events from the surface records. Figure 8a and 8c show, respectively, the vertical and horizontal components of centre shot. First arrivals are direct waves and head waves. Hyperbolas are caused by reflectors in the subsurface. Groundroll travels at lower velocities, cutting through the hyperbolas in the time record.

Shot record migration

The second step is reverse-time migration of shot records, which contains forward modelling, reverse-time extrapolation of surface records, and applying ICs.

Muting groundroll here is not critical for reverse-time migration of the shrunk Marmousi2 model. There are three reasons. First, the groundroll energy will only affect the migration of near surface part. Second, groundroll in shot images will cancel each other in the next step, stacking. Third, the groundroll energy for the shrunk Marmousi2 model is relatively weak, due to the fact that the shallow part of the subsurface has very low S-wave velocities. Thus, the preprocessing of the surface record for reverse-time extrapolation is muting direct arrivals and head waves without getting rid of the groundroll in surface records (Figure 8b and 8d).

The centre shot image (Figure 9) shows subsurface structures with significant imaging

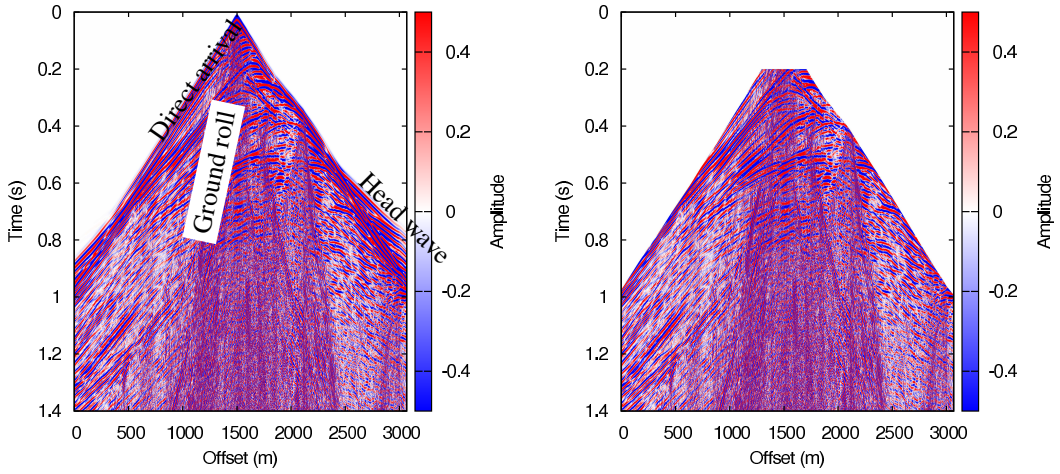

(a) Shot record: vertical component

(b) Muted record: vertical component

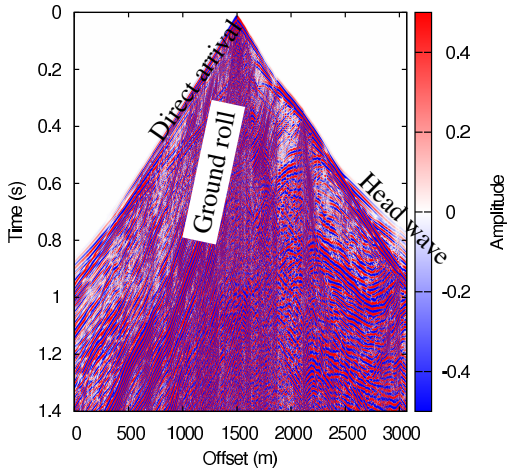

(c) Shot record: horizontal component

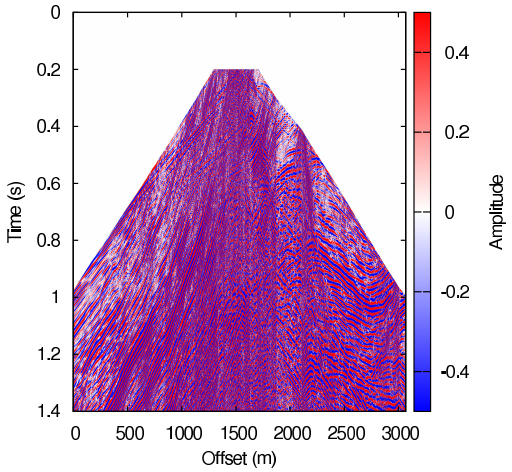

(d) Muted record: horizontal component

FIG. 8: Centre shot record of shrunk Marmousi2.

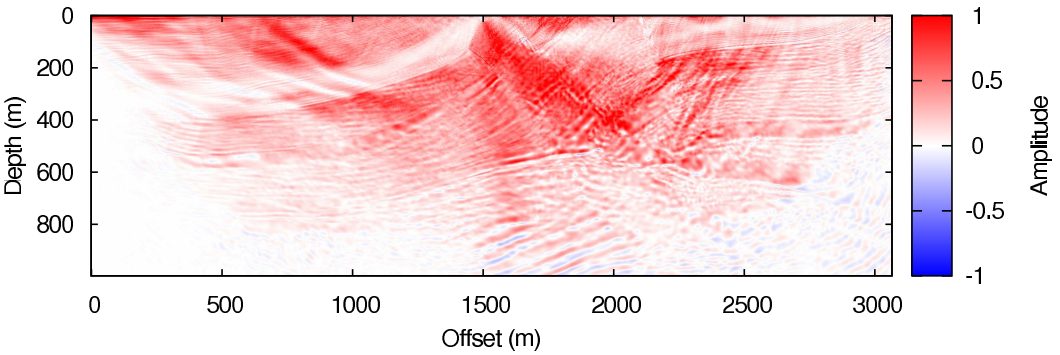

FIG. 9: Centre shot migration of shrunk Marmousi2. IC of Equation 6 is applied.

artifacts. First, image amplitudes are mostly positive values, and the overall amplitude of the upper part is higher than the bottom part. It is not surprising that stacking of shot images will have the same feature. Second, the bottom-left and bottom-right corners are not imaged or poorly imaged. This is reasonable since seismic reflections from those parts can barely reach the surface receivers. If the seismic source is put close to the left part of the surface, one can expect the image of the bottom-left corner will be improved. It is the same with the bottom-right corner. In addition to the above two features, there is some other imaging artifacts, which might be the results of poor preprocessing of the surface record before reverse-time extrapolation. For example, the rough process of muting might be one of the causes.

Stacking of shot images

The third step is stacking shot images obtained from the second step. The stack process improves signal-to-noise ratio, similar to the processing of CDP stacking.

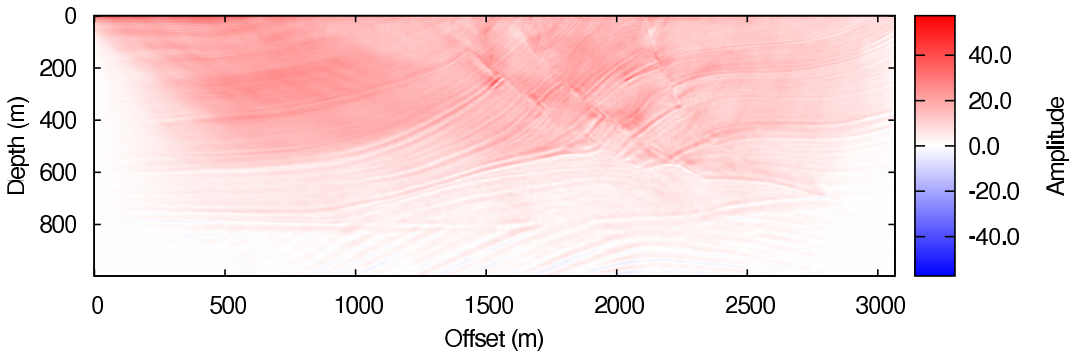

FIG. 10: Stacked RTM image of shrunk Marmousi2. It is the stack of 49 shot images.

The image shown in Figure 10 is the stacking result of 49 shots. Seismic sources are placed at lateral 50^{th} to 2450^{th} finite-difference nodes (offset from $75m$ to $3062.5m$), with distances being 50 nodes ($62.5m$). ICs of Equation 6 are applied.

Compared to the centre shot image, the areas close to bottom-left and bottom-right corners are better imaged because of higher folds. Also the subsurface structures are clearer, indicating a higher signal-to-noise ratio.

Poststack processing: highpass filtering

A fourth step of poststack processing, applying a highpass filter on the stacked image to remove the very low frequencies in the stacked image, is necessary.

Figure 11 shows results of the multicomponent prestack migration of the shrunk Marmousi2. They are obtained by the workflow described in Figure 7. Data from 49 shots are used in the prestack migration. The only difference between the images shown in Figure 11 are ICs. Each of the images corresponds to one of the source energy normalized ICs in Equation 5 or 6.

The migrated images show different features, in terms of depths of penetration and

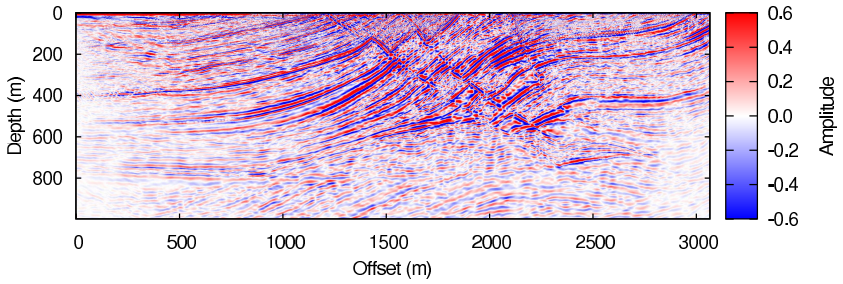

(a) HV (Equation 5c)

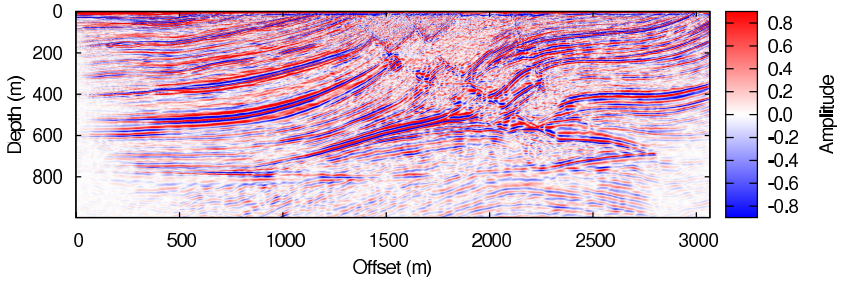

(b) HH (Equation 5d)

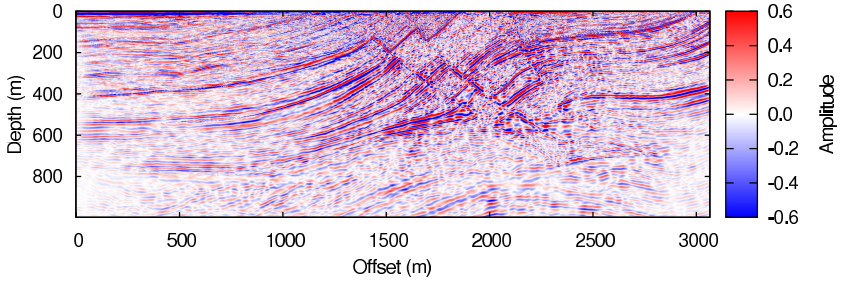

(c) VH (Equation 5b)

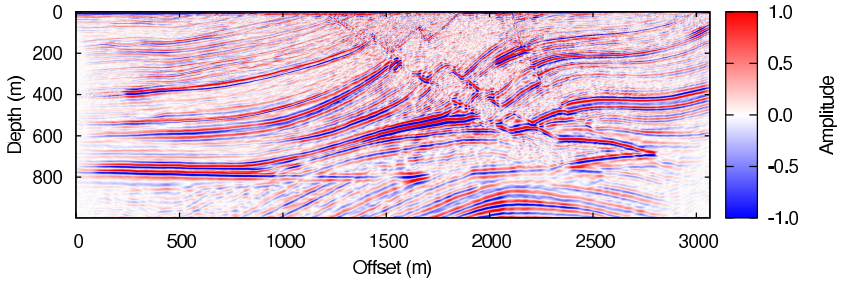

(d) VV (Equation 5a)

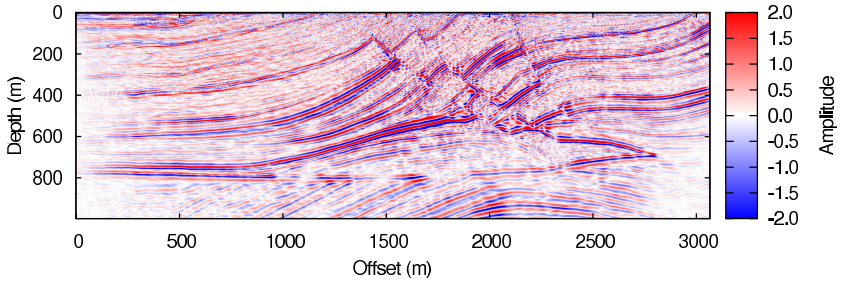

(e) Stack of above images (Equation 6)

FIG. 11: Migrated image for shrunk Marmousi2.

resolutions. These features are connected to the ICs applied.

Different ICs provide different depths of penetration with the same input data and under the same processing workflow. The VV IC (Equation 5a, see Figure 11d) provides the deepest depth of penetration among the four ICs in Equation System 5. This is reasonable: usually P waves are the main contributers to the vertical component in seismic surveys, and with faster velocities they cover deeper depths.

Different ICs provide different resolution of the subsurface geology in both the vertical and horizontal dimensions. Resolution is a measure of the ability to recognize individual, closely spaced reflectors. It is judged by image amplitudes and their continuity of the subsurface interfaces in the migrated images. In this sense, Figure 11d and 11b show better vertical resolutions than Figure 11c and 11a, while the latter two images show better horizontal resolutions. That is, the VV and HH ICs provide better vertical resolutions, while the VH and HV ICs provide better horizontal resolutions.

Figure 11e, which is the stack of Figure 11a, 11b, 11c, and 11d, shows the best image. First, it shows the deepest depth of penetration. Second, it shows the best resolution in both the vertical and horizontal dimensions. And third, as a result, it shows the highest signal-to-noise ratio overall. Thus, the stacking IC (Equation 6) is the best in all of the five proposed source energy normalized ICs.

CONCLUSIONS

A new set of imaging conditions for multicomponent imaging, so-called 'source energy normalized imaging condition', is proposed. The imaging conditions suppress both strong-source effect and weak-source effect of two other imaging conditions.

It was found that groundroll suppression is not critical for RTM at all. This was proved by the shrunk Marmousi2 migration experiment. Hence, the procedure of noise attenuation in RTM may be able to exclude groundroll suppression.

FUTURE DIRECTIONS

Further studies on wave modelling and RTM would be irregular topography, efficient 3D implementation, modelling based on more advanced medium descriptions, wavefield decomposition, and applying RTM to real data.

Irregular topography

The wave modelling and RTM methods developed assume plain horizontal free surface, which is usually not true in real seismic surveys. It is necessary for one to integrate an irregular topography algorithm into the modelling method.

Efficient 3D implementation

Although some preliminary 3D modelling results has presented (Jiang, 2012), the efficiency needs to be improved.

Advanced medium descriptions

The implemented wave modelling method is based on an isotropic elastic earth description. Although an isotropic elastic model of the earth is much more accurate than an acoustic model, there are still more advanced models available.

Wavefield decomposition

The ICs discussed are based on elastic wavefields without being decomposed into P and S waves. Research on ICs based on wavefield decomposition is also an interesting direction.

Applying RTM to real data

To apply the RTM method to real data, one needs to consider more issues. First, building an accurate subsurface velocity model is critical for a migration process. Second, it is necessary to verify that noise attenuation can exclude groundroll attenuation in real data processing, although it has been shown by a numerical example that groundroll attenuation is not critical. (It is a known fact that multiple attenuation is not necessary.) Third consideration is given to data regularization and interpolation. In order to get accurate modelling and reverse-time extrapolation results, common practice in the literature is to set spatial grid step to the level of $1m$ and time grid step to the level of $0.0001s$. Usually seismic records are sparsely and irregularly sampled. Does one need to regularize and interpolate the surface records to those fine meshes? The answer is no, according to Zhu and Lines (1997). "Fortunately, reliable interpolation of missing traces is implicitly included in the reverse-time wave equation computations. This implicit interpolation is essentially based on the ability of the wavefield to 'heal itself' during propagation." Thus, explicit interpolation is not necessary for a RTM method to use sparsely and irregularly sampled seismic data as the input. This poses as another advantage of RTM.

ACKNOWLEDGEMENTS

We thank the sponsors of CREWES for their continued support.

REFERENCES

Biondi, B., and Shan, G., 2002, Prestack imaging of overturned reflections by reverse time migration: SEG Eightieth Annual Meeting Expanded Abstract, 1284–1287.

Bording, R., and Lines, L., 1997, Seismic Modeling and Imaging with the Complete Wave Equation: Society of Exploration Geophysicists publication, Tulsa, Oklahoma.

Chang, W., and McMechan, G., 1986, Reverse-time migration of offset vertical seismic profiling data using the excitation-time imaging condition: Geophysics, **51**, No. 1, 67–84.

Chang, W., and McMechan, G., 1987, Elastic reverse-time migration: Geophysics, **52**, No. 10, 1365–1375.

Chattopadhyay, S., and McMechan, G. A., 2008, Imaging conditions for prestack reverse-time migration: Geophysics, **73**, No. 3, S81–S89.

Claerbout, J., 1971, Toward a unified theory of reflector mapping: Geophysics, **36**, No. 3, 467–481.

Du, Q., Zhu, Y., and Ba, J., 2012, Polarity reversal correction for elastic reverse time migration: Geophysics, **77**, No. 2, S31–S41.

Ion, 2012, Application of reverse time migration to complex imaging problems, [Online; accessed 22-April-2012].
URL `http://www.iongeo.com/content/documents/Resource%20Center/Case%20Studies/CS_GXT_RTM_North_Sea_080201.pdf`

Jiang, Z., 2012, Elastic wave modelling and reverse-time migration by a staggered-grid finite-difference method: Ph.D. thesis, The University of Calgary.

Jiang, Z., Bancroft, J. C., and Lines, L. R., 2010, Reverse-time migration imaging with/without multiples: CREWES Research Report, **22**.

Jiang, Z., Bancroft, J. C., Lines, L. R., and Hall, K. W., 2009, Elastic prestack reverse-time migration using a staggered-grid finite-difference method: CREWES Research Report, **21**.

Kaelin, B., and Guitton, A., 2006, Imaging condition for reverse time migration: SEG Eightieth Annual Meeting Expanded Abstract, 2594–2598.

Leveille, J. P., Jones, I. F., Zhou, Z.-Z., Wang, B., , and Liu, F., 2011, Subsalt imaging for exploration, production, and development: A review: Geophysics, **76**, No. 5, WB3–WB20.

Loewenthal, D., and Hu, L., 1991, 2-methods for computing the imaging condition for common-shot prestack migration: Geophysics, **56**, No. 3, 378–381.

McMechan, G., 1983, Migration by extrapolation of time-dependent boundary-values: Geophysical Prospecting, **31**, No. 3, 413–420.

Sun, R., and McMechan, G., 1986, Pre-stack reverse-time migration for elastic-waves with application to synthetic offset vertical seismic profiles: Proceedings of the IEEE, **74**, No. 3, 457–465.

Sun, R., and McMechan, G., 1988, Nonlinear reverse-time inversion of elastic offset vertical seismic profile data: Geophysics, **53**, No. 10, 1295–1302.

Whitmore, N., 1983, Iterative depth migration by backward time propagation: 53rd Annual International Meeting, SEG, Expanded Abstracts, 382–385.

Whitmore, N., and Lines, L., 1986, Vertical seismic profiling depth migration of a salt-dome flank: Geophysics, **51**, No. 5, 1087–1109.

Yan, J., and Sava, P., 2007, Elastic wavefield imaging with scalar and vector potentials: SEG San Antonio 2007 Annual Meeting Expanded Abstract, 2150–2154.

Zhu, J., and Lines, L., 1997, Implicit interpolation in reverse-time migration: Geophysics, **62**, No. 3, 906–917.